Available online at www.sciencedirect.com
ScienceDirect
Journal of Magnesium and Alloys xxx (xxxx) xxx
www.elsevier.com/locate/jma

Full Length Article

Effect of solute atom adsorption on heterogeneous nucleation by *in-situ* MgO particles: Experimental and theoretical studies

Liling Mo[a], Hengbin Liao[a], Xiong Zhou[a], Yu-Jun Zhao[b,*], Jun Du[a,*]

[a] *Department of Metallic Materials, School of Materials Science and Engineering, South China University of Technology, 381 Wushan Rd, Guangzhou, Guangdong 510640, China*

[b] *Department of Physics, South China University of Technology, 381 Wushan Rd, Guangzhou, Guangdong 510640, China*

Received 1 November 2021; received in revised form 7 March 2022; accepted 14 March 2022
Available online xxx

Abstract

The introduction of oxide inclusions during the smelting process has a clear promising heterogeneous nucleation potency on Mg-based alloys, but the mechanism has not been explored clearly yet. In the present work, the grain refinement mechanism of MgO in pure Mg, Mg-3Al and AZ31 (Mg-2.9Al-0.9Zn-0.3Mn) alloys is investigated by combing first-principles calculations and experiments. The theoretical results show that solute atoms adsorption will affect the nucleation and the subsequent growth process, which is an important factor affecting the refinement efficiency. A contradiction between the experimental results and the grain growth restriction factor (GRF) theory is observed, that is the refinement ratio of AZ31 is worse than Mg-3Al alloy. This is explained by an adsorption model which reveals that Al promotes the adsorption of Mg on MgO surface so as to stimulate more particles available as nucleating sites. Meanwhile, Fe and Mn also have favorable effects on the adsorption of Mg, Zn may play the opposite role compared to Al. The theoretical analyzes provide a strong support to the experiments that Al benefits the initial nucleation of α-Mg on MgO to promote the grain refining effect of Mg-3Al prior to AZ31 alloy.

Keywords: Magnesium alloy; First-principles calculation; MgO; Grain refinement; Adsorption.

1. Introduction

Magnesium (Mg) and its alloys have attracted extensive attention for their excellent properties, and are considered to have broad application prospects in industry [1–3]. However, some undesirable properties such as low mechanical properties and poor workability limit their wider applications and developments. Grain refinement can simultaneously improve the mechanical properties and processing abilities of Mg-based alloys and further broaden their applications effectively [4].

Over the past decades, some grain refinement techniques have been developed [5–10]. Nevertheless, many researchers and organizations are still striving for an efficient and stable refining method. Among them, most of the attempts are concentrated on adding nonmetallic particles or making them *in-situ* form in the Mg melt [4,11,12]. Noting that Mg has a high tendency to oxidize and will produce oxide inclusions during smelting process. Various studies have shown that oxides can act as inoculation refiners and reduce the grain size of Mg alloys effectively. Fu et al. [13] studied the refining effect of ZnO by experiments and the edge-to-edge matching (E2EM) model. They found the amounts of ZnO would be reduced by the reaction of ZnO + Mg → MgO + Zn and the grain refinement efficiency was limited. Men et al. [14] used the intensive melt shearing method to investigate the grain refinement mechanism of AZ91 alloys, where the dispersive MgO particles in the melt were thought to be potent nucleation sites. Wang et al. [15] carried out transmission electron microscope (TEM) studies, revealing that there are interfa-

* Corresponding authors.
E-mail addresses: zhaoyj@scut.edu.cn (Y.-J. Zhao), tandujun@sina.com (J. Du).

https://doi.org/10.1016/j.jma.2022.03.015

Please cite this article as: L. Mo, H. Liao, X. Zhou et al., Effect of solute atom adsorption on heterogeneous nucleation by in-situ MgO particles: Experimental and theoretical studies, Journal of Magnesium and Alloys, https://doi.org/10.1016/j.jma.2022.03.015

cial orientation relationships between α-Mg and MgO during solidification of $[2\bar{1}\bar{1}0]_{Mg}$ $(0001)_{Mg}$ || $[011]_{MgO}$ $(1\bar{1}1)_{MgO}$ and $[\bar{1}2\bar{1}3]_{Mg}$ $(1\bar{1}01)_{Mg}$ || $[110]_{MgO}$ $(\bar{1}\bar{1}1)_{MgO}$. However, there still exist some ambiguous questions about the mechanism of oxide inoculation process, which is difficult to be observed by experiments. In recent years, theoretical calculation has attracted more and more attention and is used to assist experimental research. The first-principles calculation method has been applied to study surface and interface properties between heterogeneous nuclei and substrates [16–20]. Several research groups have investigated the interface properties theoretically, such as ZnO/Mg [21], MgO/Mg [22], and so on.

Most of experiments and theoretical calculations have been carried out from the perspective of interface properties so far. Besides, there are no stable refiners for α-Mg till now. This may be actually critical to the high activity of Mg melt and the effect of solute atoms adsorption on the heterogeneous nucleation particles. The influence of solute atoms on heterogeneous nucleation process was discussed by the interdependence theory in experiments frequently [23–26]. Furthermore, the adsorption of solute atoms on nuclei surface during the initial nucleation stage is worthy to be thought profoundly. Cantor and Kim [27,28] developed a model for atomic adsorption on heterogeneous nucleation. They pointed out that the adsorption during the solidification process will affect the efficiency of nuclei as well as the subsequent grain growth process. Therefore, the common alloying and impurity elements may affect the structural stability and performance of nucleating catalyst, including Ca, Al, Zn, Mn, Fe, etc. Yao et al. [29] and Wei et al. [30] studied the influence of Mn and Fe adsorption on Al_4C_3 (0001) surface through first-principles calculations. Yang et al. used density functional theory (DFT) method to analyze the influence of Ca on Al_4C_3 [31], Al_2MgC_2 [32] and $MgAl_2O_4$ [33]. According to these simulations, adsorbed atoms will change the surface configuration of nuclei, which in turn affect their heterogeneous nucleation performance.

Following studies in the past years, it is clear that MgO can be the potent heterogeneous nucleation for α-Mg grain [14,15,22,34]. Besides, it is easy to form MgO during the smelting process. Al/Zn/Mn are the main additive elements in commercial Mg alloys, such as AZ and AM series alloys. While Fe is the inevitable impurity element during the smelting process [35]. It is believed that the existence of the solute elements has an indispensable influence on the grain refinement efficiency. Unfortunately, the adsorption details of the solute atoms on MgO surface are not well studied, leading to a blurry picture on the initial heterogeneous nucleation process.

Here, we aim to investigate the influence of solute atoms (including Al, Zn, Mn and Fe) on inoculation potency of MgO in Mg-based alloys by combining experiments and theoretical calculations. The adsorption and co-adsorption of Al, Zn, Mn, Fe and Mg on MgO surface are simulated. We demonstrate that solute atoms adsorption will affect the nucleation and the subsequent growth process, consequently affecting the grain refinement efficiency. The current work provides a theoretical insight to better understand the grain refinement mechanism of Mg-based alloys inoculated by oxide inclusions.

2. Experiments and theoretical calculations

2.1. Experimental procedures

Pure Mg, Mg-3Al, and commercial AZ31 (Mg-2.9Al-0.9Zn-0.3Mn) (wt.%, the same below) alloys were chosen as experimental materials in this work. Here, pure Mg (99.95%) and AZ31 were provided by Shanxi Regal Advanced Materials Co., Ltd., China. High purity aluminum (99.99%) was provided by ZhongNuo Advanced Material (Beijing) Technology Co., Ltd., China. Mg-3Al was synthesized by using pure Mg and high purity Al. Two series of experiments were designed, i.e., pure Mg, Mg-3Al and AZ31 alloys without or with inoculation. For alloys with inoculation, the melt was treated by *in-situ* oxidation process, in which the mixed gas of O_2 and Ar was introduced to make the oxide inclusions *in-situ* formed. According to reference [36], the gas flow rates of O_2 and Ar were set to be 10 and 100 ml/min, the rotor flowmeter was used to control the flow.

Firstly, the raw materials with different compositions (250 g in total) were placed into the MgO crucible and melted in a resistance furnace under a mixed protective atmosphere of 99.5 vol.% N_2 and 0.5 vol.% SF_6. Then the melt was untreated or inoculated for 10 min, and finally poured into a cylindrical low carbon steel mold (ϕ 40 mm × 60 mm) preheated to 500 °C. Here, the casting temperature was maintained at 760 °C. Afterwards, all the ingots were sectioned, ground, polished, and etched by the picric acid solution (picric acid 2.1 g, acetic acid 5 ml, ethanol 40 ml and water 5 ml).

Grain morphologies were observed by optical camera. Then the microstructure of the samples and the heterogeneous nuclei were characterized via scanning electron microscope (SEM, Quanta 200) equipped with energy-dispersive X-ray spectroscopy (EDS). The chemical concentrations of samples were determined via the inductively coupled plasma spectrometry (ICP, Agilent 5100). According to ASTM E112-88, average grain size was evaluated by the linear intercept method. For pure Mg, the grain size was evaluated by rings taken along different diameters of samples. The columnar crystal width was used to characterize the grain size. For Mg-3Al and AZ31, the area for measurement was the inner region of the samples with a diameter of ϕ 30 mm. Grain refining ratio (δ) was obtained by Eq. (1):

$$\delta = \frac{\text{Average grain size before inoculation} - \text{Average grain size after inoculation}}{\text{Average grain size before inoculation}} \times 100\% \quad (1)$$

2.2. Computational details

Based on density functional theory (DFT), all the first-principles calculations were conducted by the Vienna *ab initio* simulation package (VASP) [37]. The exchange-correlation

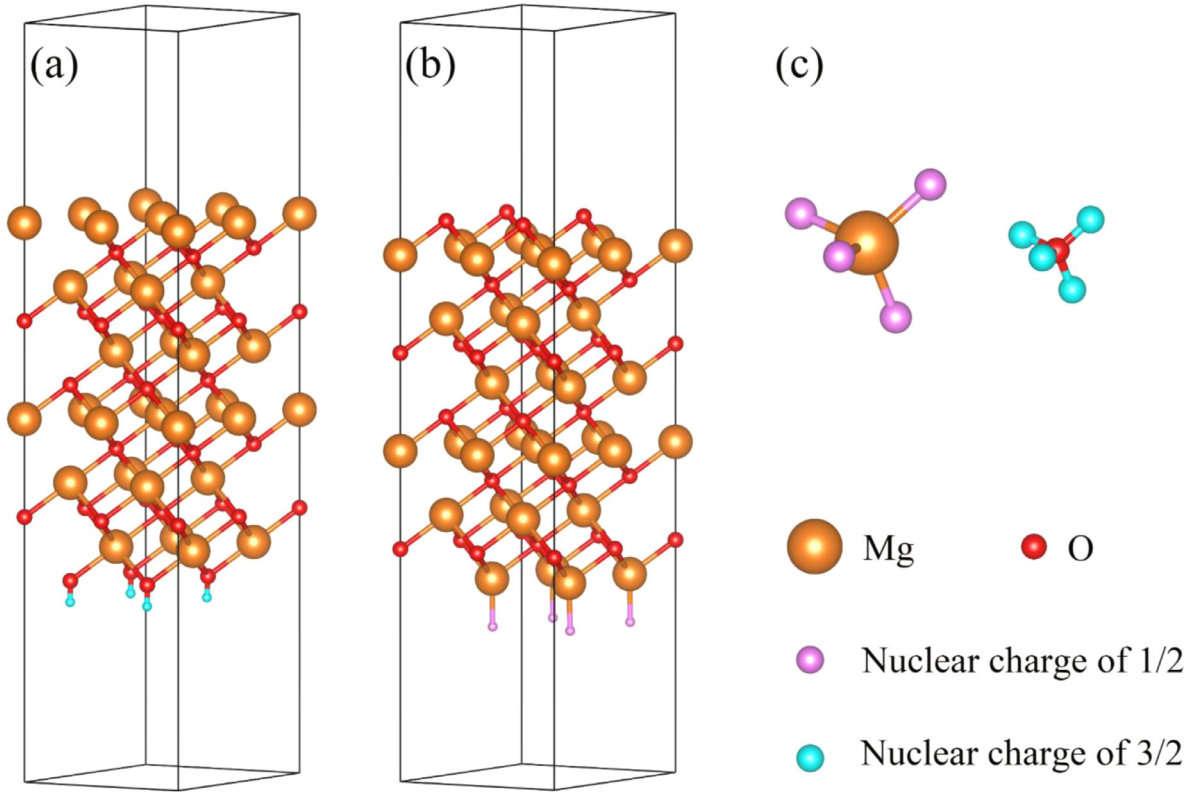

Fig. 1. MgO $(1\bar{1}1)$ surfaces saturated by the pseudo-hydrogen: (a) Mg-terminated and (b) O-terminated MgO polar surfaces; (c) Structure of the pseudo-molecule (MgH_4 and OH_4).

functional was described by the generalized gradient approximation and Perdew-Burke-Ernzerhof (GGA-PBE) [38]. The interaction between the ions and the electrons was described by the standard frozen-core potentials, which were characterized by 3*s* valence state for Mg atom, 2*s*, 2*p* for O atom, 3*s*, 3*p* for Al atom and 3*d*, 4*s* for Zn/Mn/Fe atoms, respectively. Spin polarization was considered when the magnetic atoms of Fe or Mn were involved. The kinetic energy of the plane wave was set to 520 eV based on convergence tests. Brillouin zone was sampled with $9 \times 9 \times 6$ and $9 \times 9 \times 1$ Monkhorst-Pack k-point meshes for the bulk and slab calculations. All the atomic positions were fully optimized until the force was converged to 0.03 eV/Å for each atom, and the total energy change criterion was chosen to 1×10^{-5} eV/atom.

MgO exhibits the NaCl type simple cubic structure, with the space group of $Fm\bar{3}m$ (No. 225). The relaxed lattice parameters are $a = b = c = 4.247$ Å, which is consistent with experimental data (for $a = b = c = 4.217$ Å). According to the previous studies, {100} and {111} MgO facets were observed in Mg alloys. The {111} facet is relatively stable in thermodynamics and kinetics, and its research is still inadequate. According to the TEM results, the $(1\bar{1}1)$ surface in {111} was selected for the current research [15,22,39]. A MgO $(1\bar{1}1) - (2 \times 2)$ multilayer slab model with periodic boundaries was adopted for surface simulation. MgO $(1\bar{1}1)$ surface consists of Mg and O layers alternatively aligned along the z axis. Mg-terminated and O-terminated MgO $(1\bar{1}1)$ polar surfaces were taken into consideration, as illustrated in Fig. 1(a,b). The residual internal electric field in the MgO slabs caused by the excessive atomic characteristic was weaken through the adsorption of charged substances, like pseudo-hydrogens [17]. 1/2 and 3/2 artificial hydrogen atoms were added to the surface layer atoms for both O-termination and Mg-termination, respectively (as shown in Fig. 1). The vacuum thickness was set to 15 Å. It is known that the polarized ideal surfaces are likely unstable and often undergo a surface reconstruction [40]. Here, the reconstruction is not considered as the polarized surfaces appear as part of the interface in the final models.

3. Results and discussion

3.1. Grain refinement of Mg alloys

Fig. 2 shows the macro grain morphologies of pure Mg, Mg-3Al and AZ31 alloys without or with inoculation. Fig. 3 is the corresponding average grain size and grain refining ratio. Pure Mg possesses coarse columnar structure, as shown in Fig. 2(a). Noting that only the average width of columnar structure was counted to analyze the effect of oxide inoculation, similar method has been applied in the literature [26]. The Mg-3Al and AZ31 alloys exhibit an equiaxed crystal morphology, with the average grain sizes of 1140 μm and 1612 μm, respectively. All of the alloys show an effective refinement after inoculation, as shown in Fig. 2 and Fig. 3.

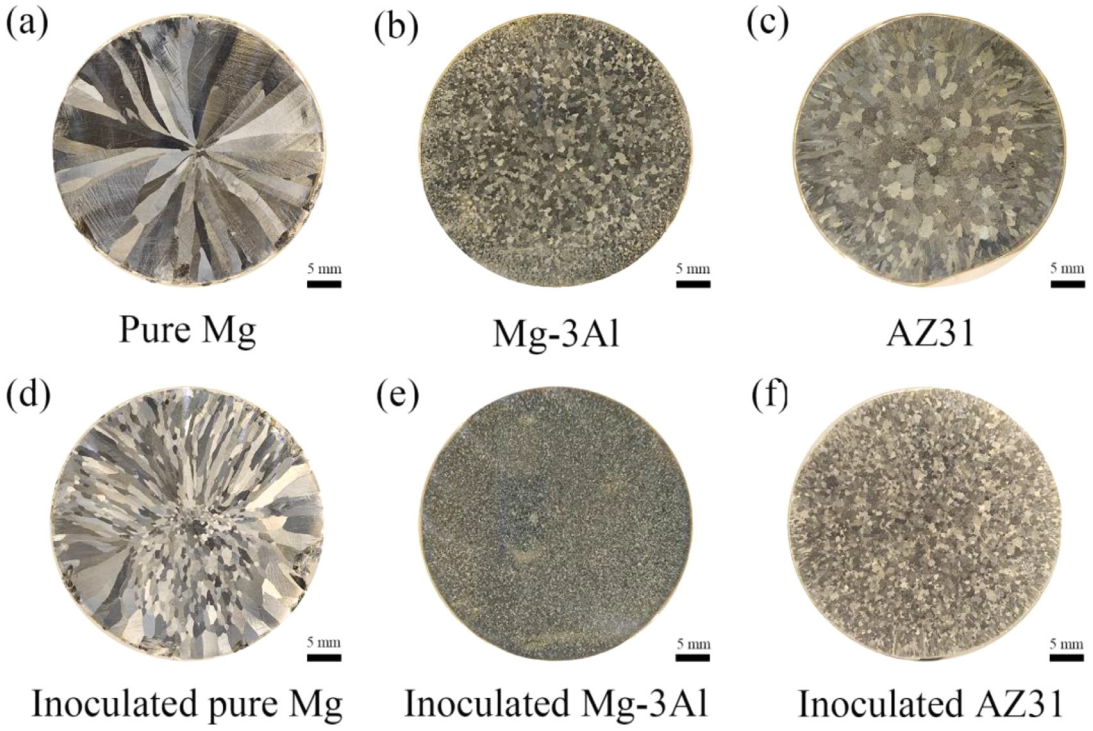

Fig. 2. Grain morphologies of as-cast pure Mg, Mg-3Al and AZ31 alloys without and with inoculation by *in-situ* oxidation process.

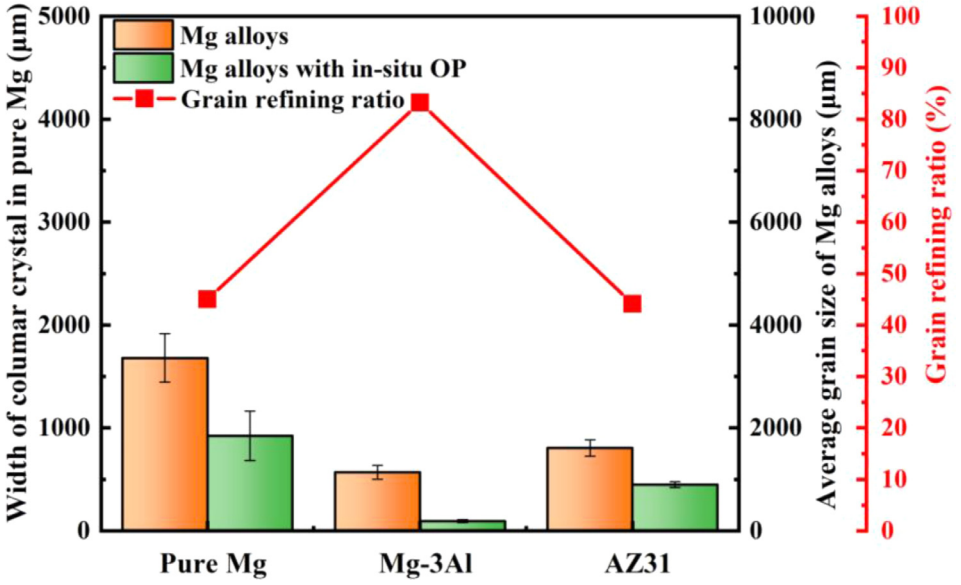

Fig. 3. Average grain size and corresponding grain refining ratio of pure Mg, Mg-3Al and AZ31 alloys without and with inoculation by *in-situ* oxidation process.

The relative grain refining ratios are about 45.0%, 83.2% and 44.1%, respectively.

Fig. 4 illustrates the microstructures of pure Mg, Mg-3Al and AZ31 alloys before and after inoculation, as well as the EDS results. Pure Mg exhibits a single-phase of α-Mg matrix, as shown in Fig. 4(a). For the Mg-3Al alloy, there are two phases that detected to be α-Mg matrix and $Mg_{17}Al_{12}$ (Fig. 4(d)). Three phases are found in the commercial AZ31 alloys, which are α-Mg, $Mg_{17}Al_{12}$, and Al_8Mn_5, as shown in Fig. 4(g). Besides, there are some Zn-rich Mg-Al particles, which could be the Mg-Al-Zn ternary phase according to reference [41] or may be due to Zn atoms adsorption on $Mg_{17}Al_{12}$ surface. It is clear that MgO particles are *in-situ* formed after inoculation (see Fig. 4). Besides, some Al-rich MgO particles were produced in Al-containing Mg alloys after inoculation (see Fig. 4(e,f,h,i)). The existence of Al solute elements may lead to the formation of $MgAl_2O_4$ according to reference [36], but is not considered here for its relatively low

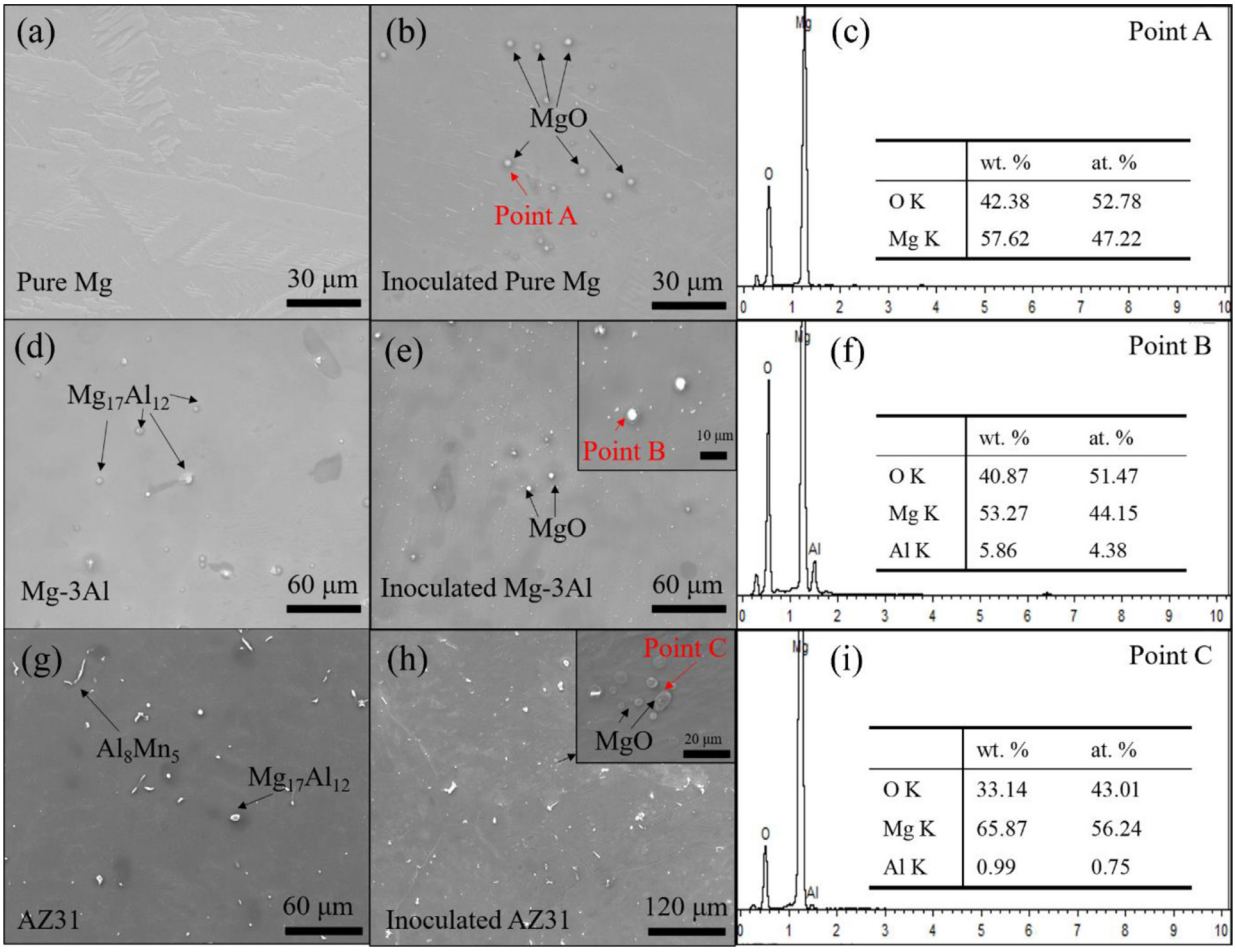

Fig. 4. Typical SEM micrographs and EDS results of as-cast pure Mg, Mg-3Al and AZ31 alloys before and after inoculation.

amount. In addition, Al_2O_3 may be formed during the melting process. However, it is unstable in the Mg melt and finally converted into MgO or $MgAl_2O_4$, similarly to other oxidation products such as MnO_2 and Fe_2O_3. In addition, the competition relationship of MgO, Al_2O_3, $MgAl_2O_4$ is analyzed from the perspective of chemical potential, as shown in Fig. 5. The results showed that in the case of Mg-rich and Al-poor (the current experimental condition), MgO is the host phase, with the chemical potential of Al increases, $MgAl_2O_4$ and Al_2O_3 form gradually. Due to the strong oxygen affinity of Mg, in the case of introducing oxygen into the Mg melt, MgO is easier to form than other oxide inclusions from kinetic point. Moreover, most of the oxide products observed in this experiment are MgO particles. Therefore, MgO is the primary oxide in pure Mg and Mg-based alloys with inoculation, which is confirmed to be potent heterogeneous nucleation substrate here.

According to the GRF theory [42,43], nucleation of pure Mg cannot occur by constitutional undercooling. The initial thermal undercooling generated by the mould provides the condition for the formation of grains, which further grow into columnar grains. Then the grain morphology is changed from columnar to equiaxed with alloying elements addition. In the case of being inoculated, MgO particles are *in-situ* formed and become the heterogeneous nucleation sites for α-Mg. All of the pure Mg, Mg-3Al and AZ31 show an effective refinement. It is obvious that the grain refining ratios of these alloys are different, and the ratio of Mg-3Al is significantly greater than AZ31 alloy. Generally, the grain growth restriction factor Q is greater with the solute elements increasing. Alloys with higher Q value always exhibit better refinement. Q is calculated by the formula of $Q = mc_0(k\text{-}1)$, here c_0 is the alloy's composition, $m(k\text{-}1)$ can be known from reference [44]. The chemical compositions of pure Mg, Mg-3Al and AZ31 alloys before and after inoculation can be seen in Table 1. The Q

Table 1
Chemical compositions (wt.%) of pure Mg, Mg-3Al and AZ31 alloys before and after inoculation.

Alloys	Chemical compositions				
	Al	Fe	Zn	Mn	Mg
Pure Mg	/	0.0008	/	0.0048	Bal.
Inoculated pure Mg	/	0.0012	/	0.0050	Bal.
Mg-3Al	3.0296	0.0016	0.0018	0.0050	Bal.
Inoculated Mg-3Al	3.1088	0.0010	0.0016	0.0047	Bal.
AZ31	2.9859	0.0014	0.8638	0.3228	Bal.
Inoculated AZ31	3.1131	0.0012	0.8938	0.3247	Bal.

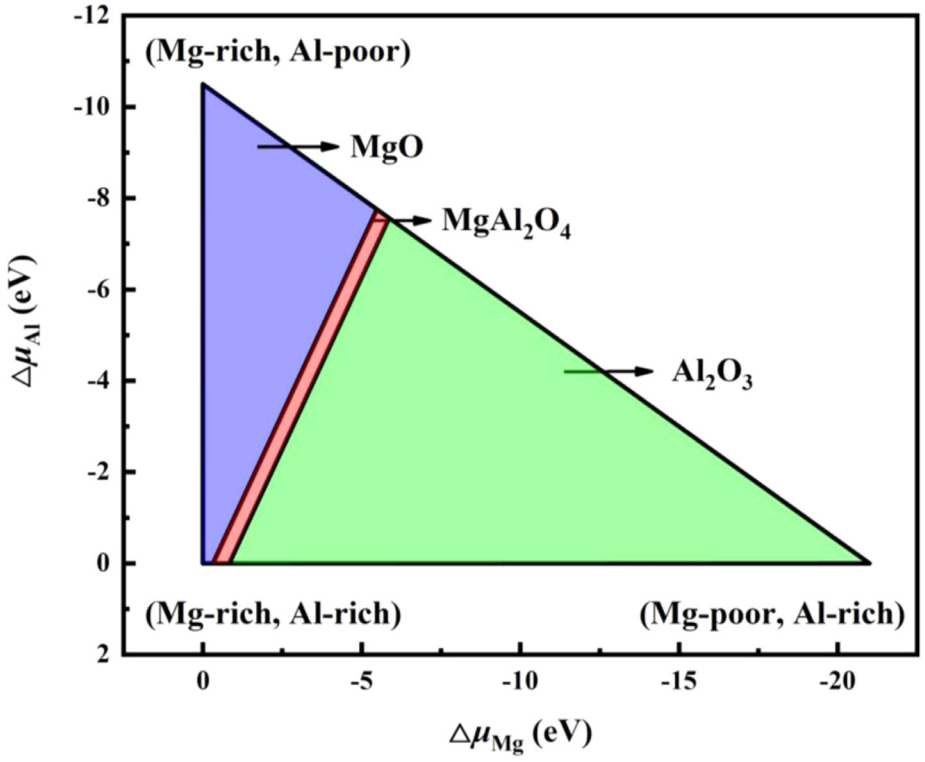

Fig. 5. Chemical potential domain calculation of Mg-Al-O system. The allowed region for $\Delta\mu_{Mg}$, $\Delta\mu_{Al}$, and $\Delta\mu_O$ at ($\Delta\mu_{Mg}$, $\Delta\mu_{Al}$) plane. All the heat of formations for the compounds are from DFT calculated results.

value of inoculated AZ31 is 0.183, which is larger than inoculated Mg-3Al of 0.135. However, the refinement ratio of AZ31 alloy is lower than Mg-3Al alloy. This is contradictory to the GRF theory.

The difference of solute elements in these samples is the most obvious change observed. Considering the solute elements are easily segregated in front of the S/L interface, thus it will adsorb on the nucleus surface and influence the adsorption of Mg during the initial stage of solidification. Besides, at the beginning of the solidification, the content of solidified Al_8Mn_5 is far less than α-Mg at the same temperature [45]. Therefore, the effect of Al_8Mn_5 on the adsorption performance is not consider here. $Mg_{17}Al_{12}$ is also excluded for the low precipitating temperature. Limited by the experimental and analytical methods, it is difficult to analyze the influence mechanism of solute atoms on the adsorption and growth process on nuclei. Therefore, the adsorption model is constructed by first-principles calculation to explore whether the solute elements Al, Zn, Mn and Fe affect the surface structure and heterogeneous nucleation of MgO.

3.2. Adsorption simulation

3.2.1. Surface properties

It is important to make sure that both Mg-terminated and O-terminated MgO $(1\bar{1}1)$ surface slabs are thick enough to stabilize the surface characteristics. Therefore, the change of interlayer spacings and corresponding surface energies of different layers were performed to determine the minimum thickness of the slab models. Surface energies of different models saturated by pseudo-H were calculated as follows [46–49]:

$$\sigma_{MgO(1\bar{1}1)} = \frac{1}{A}(E^{slab}_{MgO(1\bar{1}1)} - n\mu^{bulk}_{MgO} - n_{H_i}\hat{\mu}_{H_i}) \quad (2)$$

This is derived from the following formulas:

$$\sigma = \frac{1}{A}(E^{slab}_{MgO+H} - n_O\mu_O - n_{Mg}\mu_{Mg} - n_{H_i}\mu_{H_i} - A\sigma^{pass}_{bot}) \quad (3)$$

$$\mu_{MgO} = \mu_{Mg} + \mu_O \quad (4)$$

$$\mu^{bulk}_i + \Delta H_f(MgO) \le \mu_i \le \mu^{bulk}_i \quad (5)$$

$$\hat{\mu}_{H_i} = \frac{1}{4}\left[E_{tot}(pseudo-molecule) - \mu_i\right] \quad (6)$$

$$\hat{\mu}_{H_i} = \mu_{H_i} + \frac{A}{nH_i}\sigma^{pass}_{bot}, \quad (7)$$

where E^{slab}_{MgO+H} represents the total energy of the surface configuration passivated by pseudo-H, n_i is the number of Mg or O atoms of the slabs, σ^{pass}_{bot} is the surface energy of bottom surface passivated by pseudo-H, A is the surface area of MgO $(1\bar{1}1)$ slab. μ_i, μ_{MgO}, and $\hat{\mu}_{H_i}$ denote the chemical potential of Mg or O atoms, MgO bulk, and pseudo-H atoms, respectively. E_{tot}(pseudo-molecule) is the total energy of pseudo-molecule

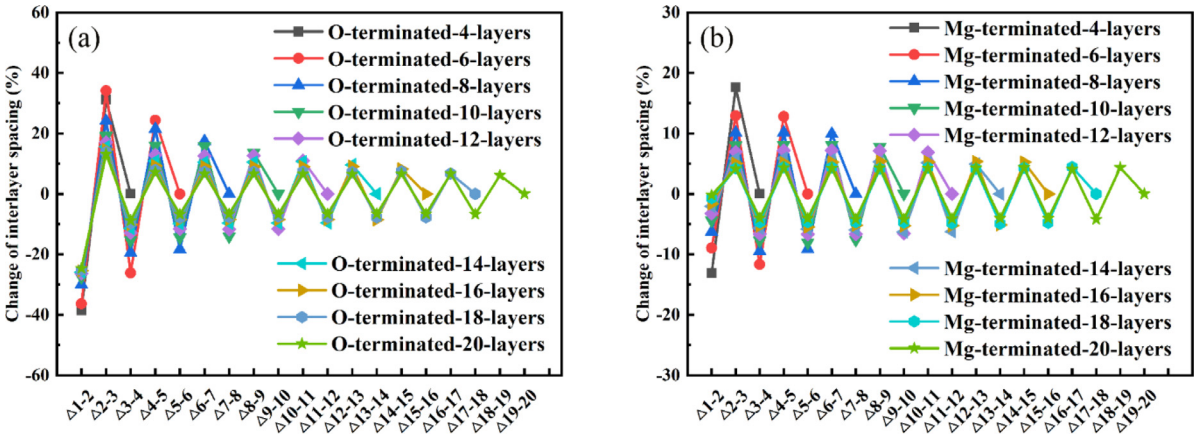

Fig. 6. The changes of interlayer spacing of MgO polar surfaces saturated with pseudo-H: (a) O-terminated and (b) Mg-terminated MgO $(1\bar{1}1)$ surface.

Table 2
The surface energies of Mg-terminated and O-terminated MgO $(1\bar{1}1)$ surface slabs.

σ (J/m^2) (Mg-terminated MgO $(1\bar{1}1)$ surface)					
$\Delta\mu_{Mg}$ (eV)	4-layers	6-layers	8-layers	10-layers	12-layers*
0	7.32	7.56	7.68	7.77	7.83
−5.48	10.13	10.37	10.49	10.58	10.65
$\Delta\mu_{Mg}$ (eV)	14-layers	16-layers	18-layers	20-layers	
0	7.85	7.92	7.94	7.96	
−5.48	10.66	10.72	10.73	10.77	
σ (J/m^2) (O-terminated MgO $(1\bar{1}1)$ surface)					
$\Delta\mu_{Mg}$ (eV)	4-layers	6-layers	8-layers	10-layers	12-layers*
0	9.46	10.49	11.14	11.48	11.68
−5.48	6.65	7.68	8.32	8.67	8.87
$\Delta\mu_{Mg}$ (eV)	14-layers	16-layers	18-layers	20-layers	
0	11.84	11.92	12.01	12.06	
−5.48	9.03	9.11	9.20	9.25	

The symbol "*" indicates that layer meets the convergence criterion and was adopted for the latter calculations.

(OH_4 or MgH_4), as shown in Fig. 1(c). ΔH_f(MgO) is the formation enthalpy of MgO bulk at 0 K, defined by the formula $\Delta H_f(\mathrm{MgO}) = \mu_{\mathrm{MgO}}^{\mathrm{bulk}} - \mu_{\mathrm{Mg}}^{\mathrm{bulk}} - \frac{1}{2}\mu_{\mathrm{O_2}}^{\mathrm{gas}}$. The corresponding result is −5.48 eV

The calculated changes of interlayer spacings are shown in Fig. 6 and the surface energies of optimized MgO $(1\bar{1}1)$ surface slabs with different thickness are listed in Table 2. It shows that as the layer thickness increases, the change of the interlayer spacing for both Mg-terminated and O-terminated surfaces decreases gradually. Meanwhile, corresponding surface energies of these different slabs are well converged (as listed in Table 2). The differences of surface energies between the 10th-layer and 12th-layer are 0.01 eV/Å^2 ($\Delta\sigma_{10\text{-}12}$=0.2 J/m^2 both for Mg-rich and O-rich condition) for O-termination and 0.004 eV/ Å^2 ($\Delta\sigma_{10\text{-}12}$=0.06 J/m^2 for Mg-rich and $\Delta\sigma_{10\text{-}12}$=0.07 J/m^2 for O-rich situation) for Mg-termination, respectively. Besides, the relaxation of atomic positions is also converged according to the change of interlayer spacing in Fig. 6. Therefore, 12 atomic layers Mg-termination and O-termination were selected for the subsequent investigation.

Furthermore, surface energy versus chemical potential $\Delta\mu_{Mg}$ was calculated to discuss the stability of O-terminated and Mg-terminated MgO surfaces, as shown in Fig. 7. It is clear that O-termination is energetically favored than Mg-termination under O-rich condition, while Mg-terminated surface is more stable under Mg-rich condition. Surface energies of these configurations have an intersection at $\Delta\mu_{Mg}$ = -3.74 eV, indicating that both O-terminated and Mg-terminated surfaces may exist and should be considered. Considering that the actual smelting and cooling process is in the Mg melt environment, the subsequent calculations and analyzes mainly focus on the Mg-termination.

3.2.2. *Stability for solute atoms adsorption on MgO* $(1\bar{1}1)$ *surface*

Adsorption of Al, Zn, Mn, Fe and Mg on MgO were discussed to describe the influence of these atoms on initial nucleation process of α-Mg. The 12-layers O(Mg)-terminated MgO $(1\bar{1}1)$ surfaces were adopted according to previous calculation. Four high symmetry adsorption sites i.e., H1 (Hollow site 1), H2 (Hollow site 2), T (Top site) and B (Bridge

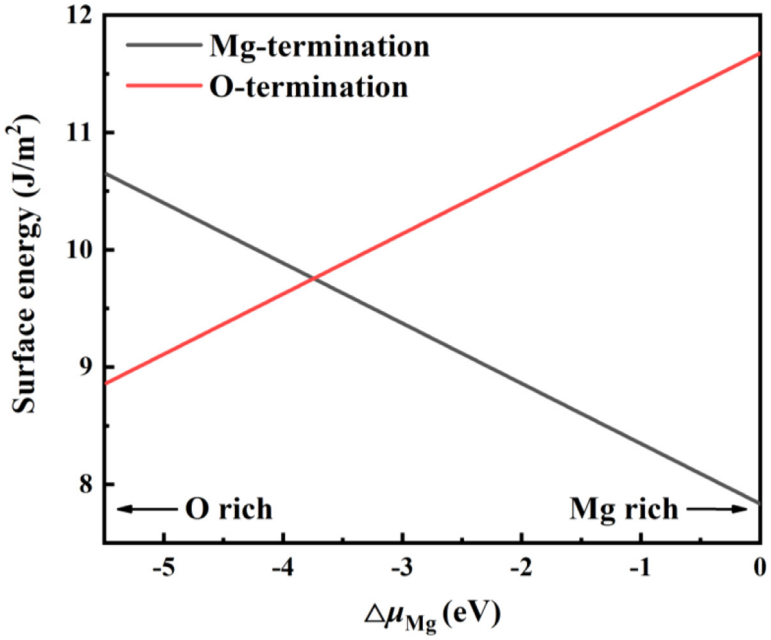

Fig. 7. Surface energies versus $\Delta\mu_{Mg}$ for O-terminated and Mg-terminated MgO $(1\bar{1}1)$ surfaces.

site), were taken into consideration. Adsorption sites of H1, H2 and T are shown in Fig. 8, while configuration of B is not shown for its instability of adsorbing Mg or solute atoms. For Mg adsorption, coverages of 0.25–1 ML were considered, only 0.25 ML and 0.5 ML for other solute atoms because the concentration of these atoms is generally low in the Mg melt. Adsorption energies of Mg or solute atoms adsorption on MgO $(1\bar{1}1)$ surfaces can be given by:

$$E_{ad} = \left[\left(E_{MgO(1\bar{1}1)} + n_i E_i\right) - E_{i/MgO(1\bar{1}1)}\right]/n_i \quad (8)$$

here $E_{MgO(1\bar{1}1)}$ is the energy of MgO $(1\bar{1}1)$ clean surface, n_i is the number of Mg or solute atoms, respectively. E_i is the energy of the isolated adatom, and $E_{i/MgO(1\bar{1}1)}$ is the total energy of MgO $(1\bar{1}1)$ surface with adatoms. The calculated individual adsorption energies of Al, Zn, Mn, Fe are listed in Table 3, while the adsorption energies of Mg on different conditions are shown in Fig. 9.

As listed in Table 3, the adsorption energies at site H2 are higher than other sites under 0.25 ML and 0.5 ML coverages for Al, Zn, Mn and Fe on O-termination. The initial adsorption of these atoms on T site will be relaxed to H2 spontaneously, and their x and y coordinates were fixed here to calculate the energies for comparison. With the coverage increasing from 0.25 ML to 0.5 ML, the difference in adsorption energy among H1, H2 and T sites decreases. For Mg-terminated surface, the adsorption energies at site H1 are mostly higher than other sites under 0.25 ML, while sites H1 and H2 are almost the same as the coverage increases to 0.5 ML. Similar phenomena can also be found for Mg adsorption on O-terminated and Mg-terminated MgO surfaces. With the coverage increasing, the adsorption energy for Mg decreases on O-termination while it increases on Mg-termination (as shown in Fig. 8Fig. 9).

Comparing the energies of Al, Zn, Mn, Fe adsorption on MgO surface, the adsorption energies follow the sequence of $E_{ad}(Al) > E_{ad}(Fe) > E_{ad}(Mn) > E_{ad}(Mg) > E_{ad}(Zn)$ both for O-terminated and Mg-terminated surfaces. It is clear that the adsorption energy of Al is greater than Mg cases of 0.25–1 ML and other elements on both O-termination and Mg-termination at the same adsorption sites and coverages. This indicates that Al is more easily to adsorb on MgO $(1\bar{1}1)$ surfaces, the same as Mn and Fe. As for Zn adsorption, the adsorption energy is less than Mg and other solute atoms. According to Eq. (8), the larger positive value of adsorption energy means the more stable structure. The adsorption energies of Zn are positive under different conditions, indicating that Zn is likely to have a tendency to adsorb on the MgO.

To study the effect of solute atoms on the initial nucleation process of α-Mg, co-adsorption of Mg and Al/Mn/Fe on H1 and H2 sites of Mg-terminated MgO surfaces were considered. The adsorption energy at the condition of Mg-X (X = Al, Mn, Fe) co-adsorption on the MgO $(1\bar{1}1)$ surfaces can be calculated by:

$$E_{ad} = \left[\left(E_{X/MgO(1\bar{1}1)} + n_{Mg}E_{Mg}\right) - E_{(X+Mg)/MgO(1\bar{1}1)}\right]/n_{Mg} \quad (9)$$

$E_{X/MgO(1\bar{1}1)}$is the total energy of the slab that single solute atom adsorption, and $E_{(X+Mg)/MgO(1\bar{1}1)}$ is the total energy of Mg and solute atom co-adsorption. The actual coverage of Al or Mg depends on their chemical potentials in the experiment. Here the chemical potential of Mg is about zero with respect to bulk Mg as Mg melt exists in the sample, while the chemical potential of Al will be much smaller as the content of Al is relatively small. This is corresponding to a Mg-rich and Al-poor condition in the experiment. Therefore, only the low coverage of Al is considered in this work following the

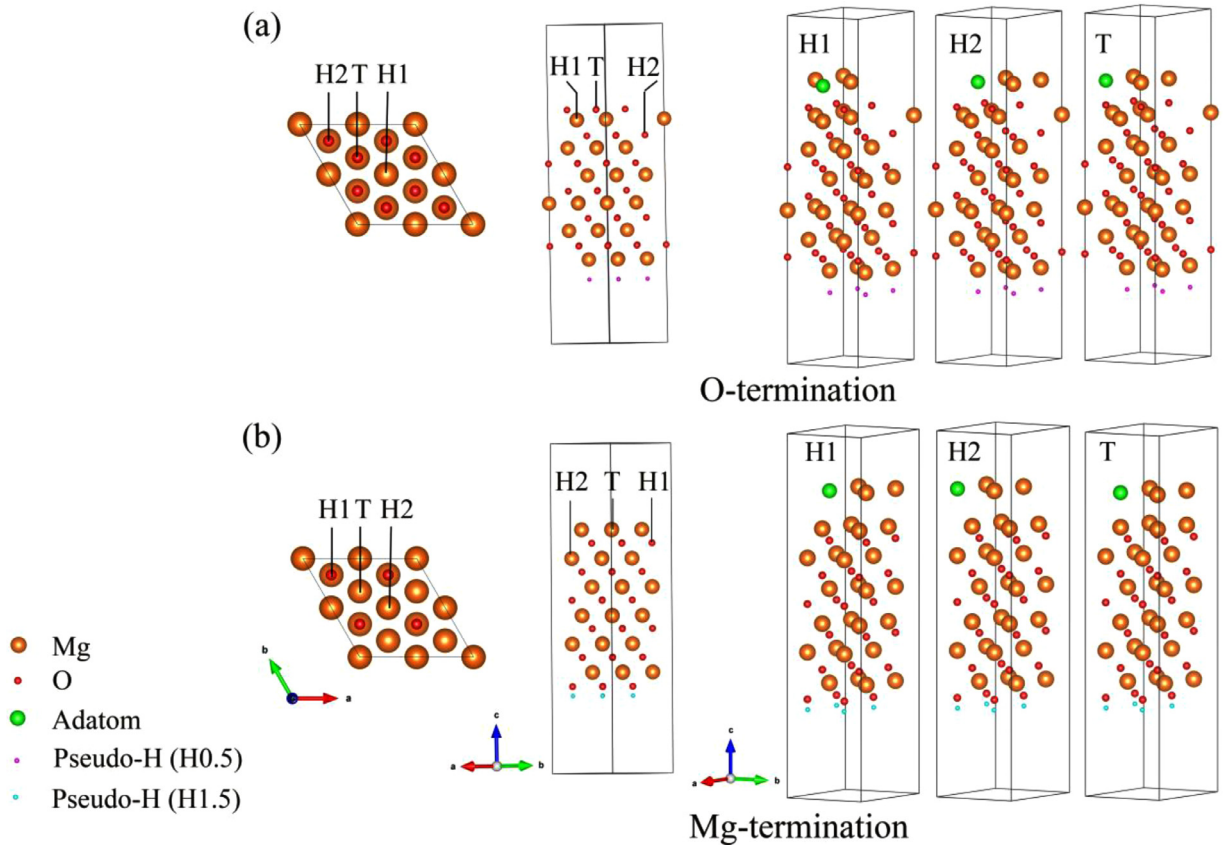

Fig. 8. The diagrammatic drawing of adsorption sites and co-adsorption on the 12-layers of (a) O-terminated and (b) Mg-terminated MgO $(1\bar{1}1)$ surfaces.

Table 3
The adsorption energies of Al, Zn, Mn and Fe atoms on O(Mg)-terminated MgO $(1\bar{1}1)$ surfaces. (F) in the Table stands for fixing the x and y coordinate of adatoms for their instability.

Termination	Coverage (ML)	Adsorption site	Adsorption energy (eV)			
			Al	Zn	Mn	Fe
O	0.25	H1	12.85	6.18	10.98	11.01
		H2	13.55	6.53	11.12	11.28
		T	7.48 (F)	3.57 (F)	6.92 (F)	6.63 (F)
	0.5	H1	9.39	4.88	7.72	7.85
		H2	9.66	5.17	7.64	8.20
		T	8.85	3.16	7.12	1.91 (F)
Termination	Coverage (ML)	Adsorption site	Adsorption energy (eV)			
			Al	Zn	Mn	Fe
Mg	0.25	H1	7.06	0.64	2.26	2.65
		H2	7.07	0.59	2.13	2.71
		T	6.97	0.31	1.84	2.25
	0.5	H1	5.50	0.81	2.38	3.01
		H2	5.50	0.83	2.38	2.95
		T	5.50	0.63	2.09	2.58

practical condition, similarly to other solute atoms. Based on above discussion and the computational cost of DFT calculations, the coverage ratio of Mg and solute atoms were selected to be 3:1 in the model construction to simulate the impact of solute atoms on the adsorption of Mg.

The calculated co-adsorption energies of Mg/Al, Mg/Mn and Mg/Fe on Mg-termination are shown in Fig. 10. There are some discrepancies on energies between different solute atoms and Mg co-adsorption. The co-adsorption energies follow the order of $E_{\text{co-ad}}(\text{MgAl}) > E_{\text{co-ad}}(\text{MgFe}) > E_{\text{co-ad}}(\text{MgMn}) > E_{\text{ad}}(1\,\text{ML Mg})$ for Mg-termination. It is obvious that all the energies of Mg/Al, Mg/Fe, Mg/Mn co-adsorption are greater than 1 ML Mg case on Mg-terminated MgO surfaces. This means that Al, Fe, Mn atoms will adsorb on MgO surface

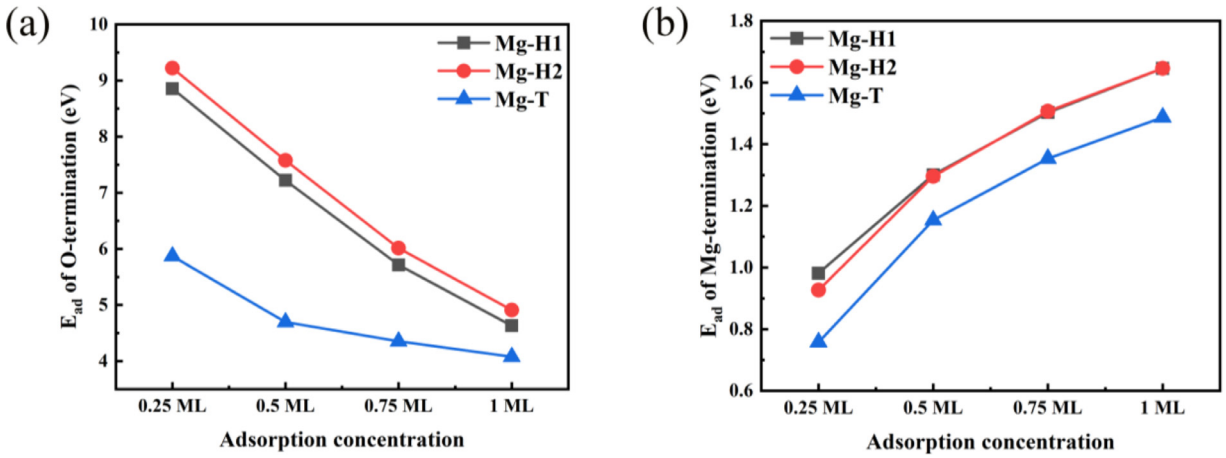

Fig. 9. The adsorption energies of Mg on (a) O-terminated and (b) Mg-terminated MgO $(1\bar{1}1)$ surfaces.

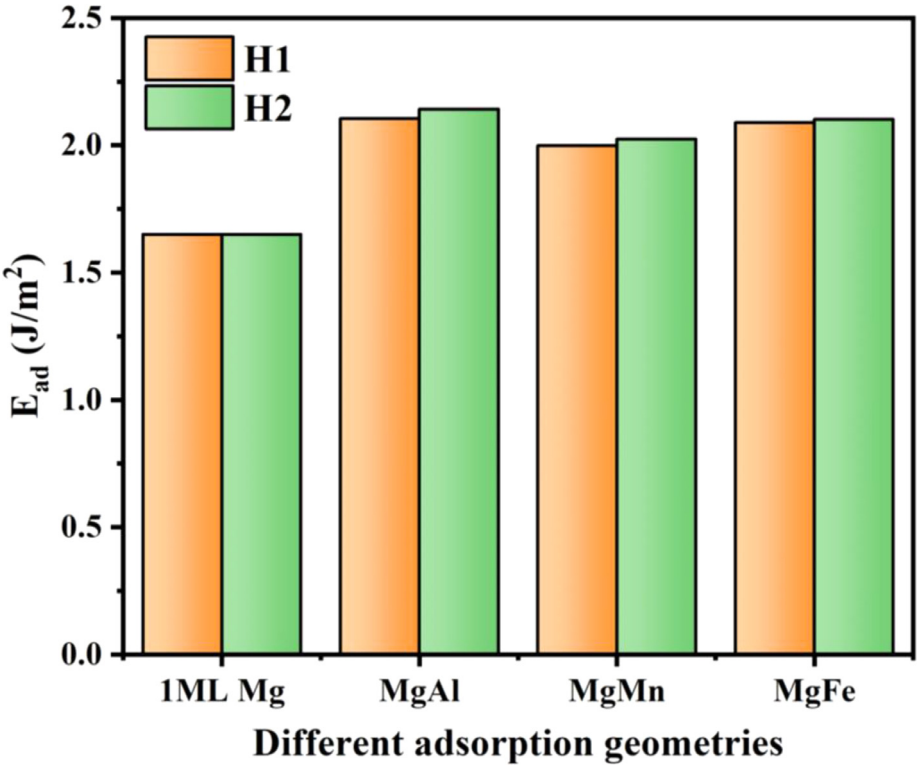

Fig. 10. The effects of Al, Fe and Mn on the adsorption energy of Mg on the Mg terminated MgO $(1\bar{1}1)$ surface.

prior to Mg, then the existence of them promotes the adsorption of Mg atoms on MgO. Therefore, more α-Mg grains are nucleating on oxide particles acting as nucleation catalyst. This will lead to the fact that the grain refining ratio of Mg-3Al is greater than pure Mg, so as to AZ31 alloy. Unfortunately, the effect of Zn on Mg adsorption is not clear from the theoretical point of view, which requires further investigation.

3.2.3. Electronic structure and bonding characteristics

The structural evolution and performance of the nuclei after adsorption are closely associated with the bonding between the adatoms and surface atoms. Therefore, to have some insight into the surface properties more intuitively from a microscopic perspective, the charge density differences (CDD) for Mg and Al/Zn/Mn/Fe adsorption and co-adsorption at H1 for Mg-termination MgO surface were calculated here. The CDD $\Delta\rho$ can be calculated as:

$$\Delta\rho = \rho_{i/MgO(1\bar{1}1)} - \rho_i - \rho_{MgO(1\bar{1}1)} \quad (10)$$

where $\rho_{i/MgO(1\bar{1}1)}$ is the electron density of the total i/MgO $(1\bar{1}1)$ adsorption system, $\rho_i$and $\rho_{MgO(1\bar{1}1)}$ are the unperturbed

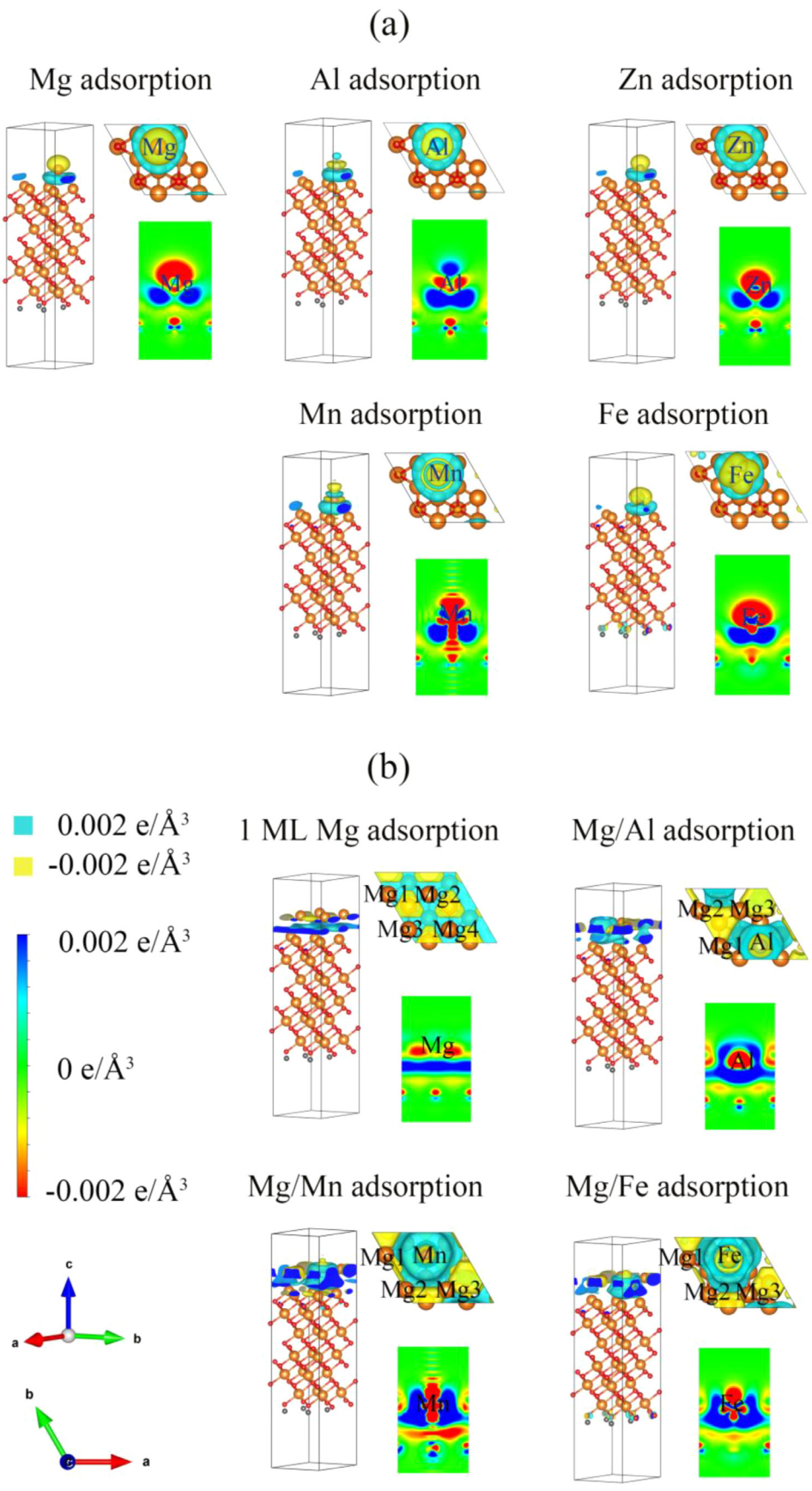

Fig. 11. Distribution of charge density differences (CDD) of Mg and Al/Zn/Mn/Fe adsorption and co-adsorption on Mg-terminated MgO $(1\bar{1}1)$ system. Here, Mg 1–4 represent the adsorbed Mg atoms in the surface model.

electron densities of isolated adatoms and MgO $(1\bar{1}1)$ surfaces, respectively.

The calculated CDDs are shown in Fig. 11. Here, the blue areas indicate charge accumulation while yellow and red areas represent charge depletion. It is worth noting that the rearrangement of the charge is mainly distributed to the adatoms and the top layer atoms on the surface. Taking Al adsorption and Mg-Al co-adsorption as an example, the CDDs of Mg and Al adsorption/co-adsorption in Fig. 11 show that the charge mainly transfers from the adatoms to the middle regions, and there are charge accumulation between Mg-Mg and Mg-Al atoms, implying that polar covalent bonds are formed between metal-metal atoms. Similar phenomena can be found for other solute atoms (Zn, Mn, Fe) adsorption on Mg-terminated surface.

Bader charge analysis was carried out to verify the charge transfer between adatoms and the top layer atoms, as shown in Fig. 12. The charges of Mg atoms on the top layers of Al/Mn/Fe adsorption models are more than those in clean surface and Mg adsorption case, and the charge of the adsorbed metallic atoms are changed for single and co-adsorption case. For the case of Mg and Al co-adsorption, the charge of adsorbed Al gains 2.47 e, which is more than single Al adsorption of 1.21 e. Besides, adatoms seem to have stronger interaction with the surface atoms compared with single adsorption case. It indicates that solute atoms adsorption preferentially would influence the bonding on the surface, then strengthen the stability of surface structure and affect the refinement efficiency of heterogeneous nuclei. The calculated results of Bader charge are consistent with the CDDs.

The density of states (DOS) and corresponding partial density of states (PDOS) were carried out to further explore the surface bonding after adsorption. Fig. 13(a) indicates that bulk MgO is an insulator with a band gap of 3.32 eV (much smaller than the experimental gap of 6.36 eV due to the well-known underestimation of GGA calculations). The surface become metallic as the band gap disappears, mainly due to the charge residual from the Mg atoms on the surface for the unstable polarized surface. After single Al adsorption, the characteristic of metallic is degraded. The resonance of PDOS with different adsorbates is observed at around $-20\sim-15$ eV and $-8\sim8$ eV Besides, it can be seen that the *s* electron of Al atoms are slightly hybridized with s/*p* electron of Mg around -5 eV for single alloying elements adsorption and co-adsorption, which shows the formation of covalent bonds between the adatoms and Mg atoms. Besides, the value of the PDOS at Fermi level for Mn, Fe and Mg adsorption and co-adsorption in the Mg-terminated system are larger than clean surface and single element adsorption, reflecting the stronger metallic feature after Mg and Mn/Fe co-adsorption on surface. In consequence, the bonding characteristic between the adsorbed metallic atoms and the surface Mg-layer atoms on the Mg-termination is mainly covalent bonds.

There are significant differences in PDOS results of different adsorption slabs, demonstrating that there are some discrepancies about the interaction between various adatoms and Mg atoms, and bond strength will be different for these atoms.

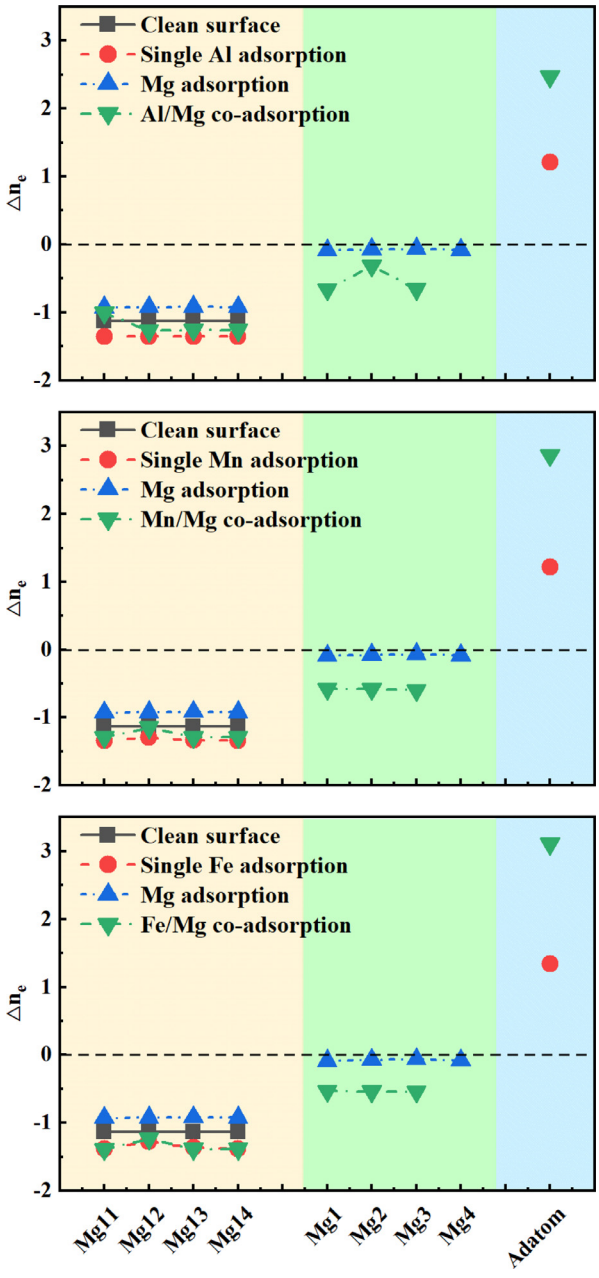

Fig. 12. Bader charge analysis of selected atoms for Al/Mn/Fe and Mg adsorption and co-adsorption on Mg-terminated MgO $(1\bar{1}1)$ surfaces (positive means get charge while negative is lost charge). Here, Mg 1–4 represent the adsorbed Mg atoms in the surface model. Mg 11–14 are Mg atoms on the top layer of MgO surface.

This indicates that adsorption of solute atoms will significantly influence the surface properties of the grain refiners, consequently influencing their inoculation performance in the initial nucleation process, in line with the experiment results.

3.3. Analysis of grain refinement mechanism

MgO was observed for *in-situ* oxidation inoculated pure Mg, Mg-3Al and AZ31 alloys, and is considered to be the heterogeneous nucleation sites in the present work. Accord-

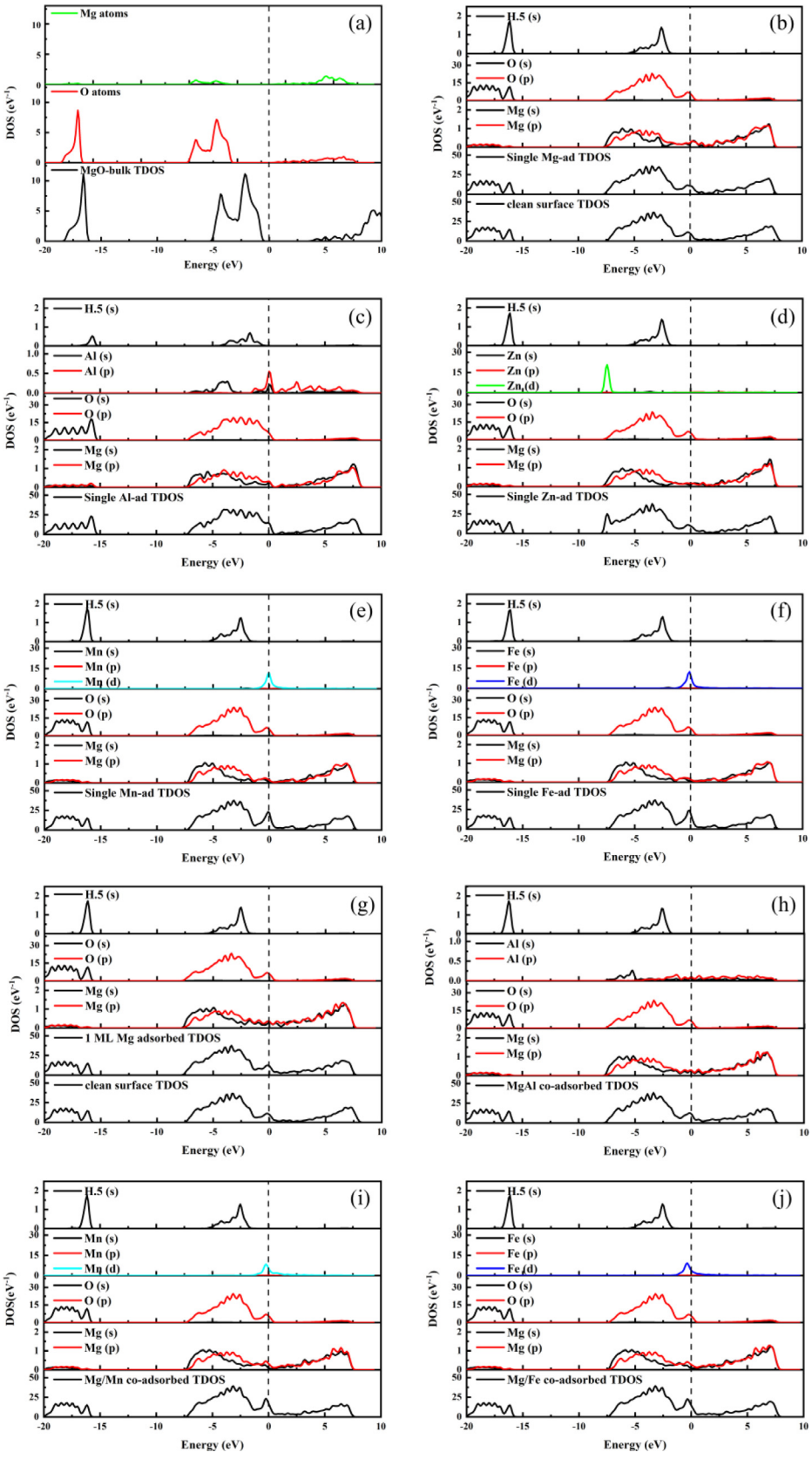

Fig. 13. (a) Density of states (DOS) of MgO bulk and corresponding projected density of states (PDOS) of Mg, O atoms; (b)-(f) Total density of states and PDOS for single Mg, Al, Zn, Mn, Fe adsorption and (g)-(h) 1 ML Mg, Mg/Al, Mg/Mn, Mg/Fe co-adsorption on Mg-terminated MgO surface, respectively. Here, dashed lines denote the Fermi level.

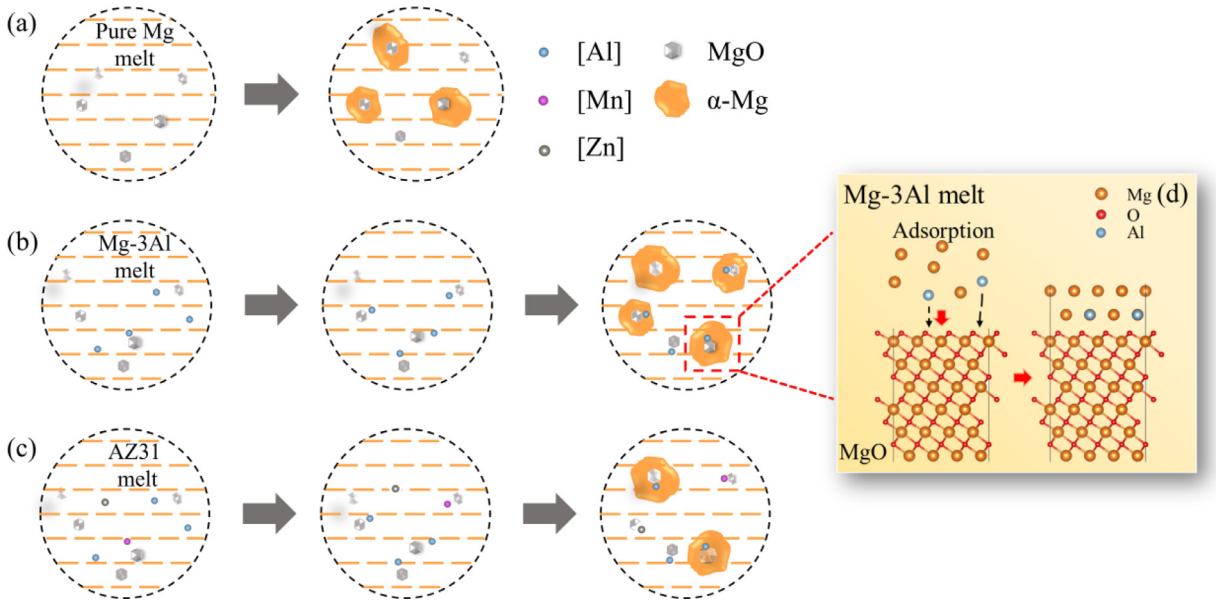

Fig. 14. (a–c) The schematic diagram of initial nucleation progress of pure Mg, Mg-3Al and AZ31 alloys inoculated by *in-situ* MgO; (d) Adsorption process of MgO surface in Mg-3Al alloy. The orange dashed lines in (a)-(c) denote the molten Mg.

ing to the interdependence theory, constitutional supercooling (CS) induced by solute elements offers an extra undercooling for heterogeneous substrates and plays an important role in connecting the nucleation and grain growth [23]. Actually, growth restriction factor Q is a calculation for development rate of the constitutional zone [43]. The addition of solute elements with a larger Q value not only increase the restricting effect for growth, but also create a stronger CS for stimulating heterogeneous nucleation, thereby increasing the grain refinement efficiency. However, we confirmed that AZ31 has a lower refinement ratio, though the Q value is larger than Mg-3Al alloy. From the perspective of the nucleation and growth process, the initial nucleation is affected by the adsorption of solute elements.

The schematic diagram of nucleation process for inoculated Mg-based alloys is shown in Fig. 14. After being inoculated, MgO particles are formed in the melt. For the inoculated pure Mg, part of the particles can be the heterogeneous sites at the beginning of solidification. As for the Mg-3Al alloy, the dissociative Al atom in the melt has a strong adsorption capacity on MgO surface in the initial nucleation process. Besides, it can be observed from Table 3 and Fig. 9 that the adsorption energy of Al is higher than Mg. For the commercial AZ31 alloy, the adsorption of Al and Mn will also increase the adsorption energy of Mg on MgO. These results suggest that Al is easier to adsorb on MgO surface than Mg. In the case of Al adsorption on Mg-terminated MgO $(1\bar{1}1)$ surface, the energies of Mg adsorption increase from 1.65 eV to 2.10 eV and 1.65 eV to 2.14 eV for H1 and H2 sites, respectively. The influence of increasing Al concentration on the calculation results of adsorption energy was considered to verified the accuracy. The co-adsorption energy was calculated when the coverage of Al is 0.5 ML. The results showed that with the coverage increases from 0.25 ML to 0.5 ML, the co-adsorption energies on Mg-termination increase from 2.10 eV to 2.25 eV and 2.14 eV to 2.33 eV for H1 and H2 sites, respectively. It is still higher than 1 ML Mg adsorption case. Since the experiment is in the Mg melt environment, the coverage of Al is not considered greater than 0.5 ML. These results provide important evidence that Al promotes the adsorption of Mg on MgO surface, and Fe and Mn seem to have weakly favorable role on the adsorption of Mg. For Zn adsorption case, because the single adsorption energy is lower than Mg, it is difficult to determine the influence of Zn on the adsorption of Mg from the view of theoretical point. According to the experimental results, it is deduced that Zn may be unfavorable to the adsorption of Mg on MgO surface, which deserved further exploration.

The above analysis implies that the grain refinement efficiency of nucleating particles is related to the effect of solute atoms on the adsorption of Mg to MgO particles surface, for Al/Mn/Fe are positive. This means that Al adsorption on MgO would significantly promote the nucleating of α-Mg and more particles available as nucleating sites, thus strengthen the ability of MgO for acting as heterogeneous nucleation substrate to a great extent, as shown in Fig. 14(d). The theoretical results provide a powerful supporting for the experimental phenomena that Al has a positive effect on the adsorption and nucleation of α-Mg grains on MgO particles, it is one of the reasons that the refinement efficiency of Mg-3Al is higher than AZ31 alloy.

4. Conclusion

Through a combination of experiments and first-principles calculations, the potent nucleant of pure Mg, Mg-3Al and AZ31 alloys inoculated by *in-situ* oxidation process has been determined. Adsorption energies, electronic structures and

bonding of Mg and Al/Zn/Mn/Fe adsorption on MgO $(1\bar{1}1)$ surface were studied. The conclusions are summarized as following:

(1) MgO is proved to have a great grain refinement effect on pure Mg, Mg-3Al, and AZ31 alloys. The refining ratio of Mg-3Al is greater than AZ31 alloy, which is contradictory to the GRF theory.
(2) Al is preferentially adsorbed on MgO surface than Mg and other solute atoms at Mg-termination and O-termination. Besides, the energies of Mg/X (X = Al/Mn/Fe) co-adsorption demonstrate that Al promotes the adsorption of Mg on MgO surface, Fe and Mn also have weakly favorable role on the adsorption of Mg.
(3) The electronic structure and bonding characteristics of the adsorption structure show that polar covalent bonds are formed between adatoms and top layers atoms, which will influence the structure and performance of the nuclei.
(4) The adsorption energy of Mg on MgO surface will change significantly after solute atoms adsorption. It concludes that solute atoms adsorb on MgO surface will affect the subsequent stacking and growth of α-Mg on MgO. Therefore, the addition of solute atoms will influence the grain refining efficiency of primary Mg grains by oxide inoculation.

Declaration of Competing Interest

The authors declare that they have no known competing financial interests or personal relationships that could have appeared to influence the work reported in this paper.

Acknowledgment

This work was supported by the National Natural Science Foundation of China (No. 51871100). Computing resources from national supercomputer center in Guangzhou are gratefully acknowledged.

References

[1] Y. Yang, X. Xiong, J. Chen, X. Peng, D. Chen, F. Pan, J. Magnes. Alloy. 9 (2021) 705–747.
[2] W.J. Joost, P.E. Krajewski, Scr. Mater. 128 (2017) 107–112.
[3] J. Song, J. She, D. Chen, F. Pan, J. Magnes. Alloy. 8 (2020) 1–41.
[4] E. Karakulak, J. Magnes. Alloy. 7 (2019) 355–369.
[5] T. Motegi, Mater. Sci. Eng. A 413-414 (2005) 408–411.
[6] P. Cao, M. Qian, D.H. StJohn, Scr. Mater. 51 (2004) 125–129.
[7] M. Qian, P. Cao, Scr. Mater. 52 (2005) 415–419.
[8] M. Easton, D. StJohn, Metall. Mater. Trans. A 30 (1999) 1613–1623.
[9] B. Nagasivamuni, G. Wang, D.H. StJohn, M.S. Dargusch, Light Met. 2019 (2019) 1579–1586.
[10] B. Nagasivamuni, K.R. Ravi, J. Alloy. Compd. 622 (2015) 789–795.
[11] D. Shepelev, J. Klempf, M. Bamberger, A. Katsman, J. Mater. Sci. 46 (2011) 5798–5806.
[12] H. Liao, M. Zhan, C. Li, Z. Ma, J. Du, J. Magnes. Alloy. 4 (2020) 1211–1219.
[13] H. Fu, D. Qiu, M. Zhang, H. Wang, P.M. Kelly, J.A. Taylor, J. Alloy. Compd. 456 (2008) 390–394.
[14] H. Men, B. Jiang, Z. Fan, Acta Mater. 58 (2010) 6526–6534.
[15] Y. Wang, Z. Fan, X. Zhou, G.E. Thompson, Philos. Mag. Lett. 91 (2011) 516–529.
[16] D.J. Siegel, L.G. Hector Jr, J.B. Adams, Surf. Sci. 498 (2002) 321–336.
[17] B. Meyer, D. Marx, Phys. Rev. B 69 (2004) 1681–1685.
[18] S. Lu, Q. Hu, R. Yang, B. Johansson, L. Vitos, Phys. Rev. B 82 (2010) 195103.
[19] Y. Liu, H. Ren, W. Hu, D. Li, X. Zeng, K. Wang, J. Lu, J. Mater. Sci. Technol. 32 (2016) 1222–1231.
[20] L. Boulley, D. Kandaskalov, M.C. de Weerd, S. Migot, J. Ghanbaja, S. Šturm, P. Boulet, J. Ledieu, É. Gaudry, V. Fournée, Appl. Surf. Sci. 542 (2021) 148540.
[21] S. Yang, J. Du, Y. Zhao, Mater. Res. Express 5 (2018) 036519.
[22] H. Song, M. Zhao, J. Li, Mod. Phys. Lett. B 30 (2016) 1650152.
[23] D.H. StJohn, M. Qian, M.A. Easton, P. Cao, Acta Mater. 59 (2011) 4907–4921.
[24] D.H. StJohn, M.A. Easton, M. Qian, P. Cao, M.J. Bermingham, Mater. Sci. Forum 690 (2011) 206–209.
[25] C. Li, S. Yang, J. Du, H. Liao, G. Luo, J. Magnes. Alloy. 8 (2020) 1090–1101.
[26] N. Balasubramani, G. Wang, M.A. Easton, D.H. StJohn, M.S. Dargusch, J. Magnes. Alloy. 9 (2021) 829–839.
[27] W.T. Kim, B. Cantor, Acta Metall. Mater. 42 (1994) 3115–3127.
[28] B. Cantor, G.W. Greenwood, A.L. Greer, D.M. Herlach, K.F. Kelton, Ser. A Math. Phys. Eng. Sci. 361 (2003) 409–417.
[29] L. Yao, K. Li, N. Zhou, Appl. Surf. Sci. 363 (2016) 168–172.
[30] C. Wei, K. Li, L. Yao, N. Zhou, Mater. Res. Express 4 (2017) 106517.
[31] S. Yang, C. Li, J. Du, Y. Zhao, Appl. Surf. Sci. 491 (2019) 187–194.
[32] S. Yang, C. Li, J. Du, Y. Zhao, Mater. Des. 192 (2020) 108664.
[33] S. Yang, C. Li, G. Luo, J. Du, Y. Zhao, J. Alloy. Compd. 861 (2021) 158564.
[34] Z. Fan, Y. Wang, M. Xia, S. Arumuganathar, Acta Mater. 57 (2009) 4891–4901.
[35] S. Jayasathyakawin, M. Ravichandran, N. Baskar, C. Anand Chairman, R. Balasundaram, Mater. Today Proc. 27 (2020) 909–913.
[36] H. Liao, L. Mo, X. Zhou, B. Zhao, J. Du, J. Mater. Res. Technol. 12 (2021) 807–817.
[37] G.G. Kresse, J.J. Furthmüller, Phys. Rev. B 54 (1996) 11169.
[38] J.P. Perdew, K. Burke, M. Ernzerhof, Phys. Rev. Lett. 77 (1996) 3865–3868.
[39] S. Wang, Y. Wang, Q. Ramasse, Z. Fan, Metall. Mater. Trans. A 51 (2020) 2957–2974.
[40] Y. Liu, W. Xu, Y. Shan, H. Xu, J. Phys. Chem. C 121 (2017) 15711–15718.
[41] Y. Ren, G. Qin, W. Pei, S. Li, Y. Guo, H. Zhao, Trans. Nonferr. Met. Soc. China 22 (2012) 241–245.
[42] A.L. Geer, A.M. Bunn, A. Tronche, P. Evans, Acta Mater. 48 (2000) 2823–2835.
[43] M.A. Easton, D.H. StJohn, Acta Mater. 49 (2001) 1867–1878.
[44] D.H. StJohn, M. Qian, M.A. Easton, P. Cao, Z. Hildebrand, Metall. Mater. Trans. A 36A (2005) 1669–1679.
[45] T. Chen, Y. Yuan, T. Liu, D. Li, A. Tang, X. Chen, R. Schmid-Fetzer, F. Pan, JOM 73 (2021) 892–902.
[46] Y. Zhang, J. Zhang, K. Tse, L. Wong, C. Chan, B. Deng, J. Zhu, Sci. Rep. 6 (2016) 20055.
[47] J. Zhang, Y. Zhang, K. Tse, B. Deng, H. Xu, J. Zhu, J. Appl. Phys. 119 (2016) 205302.
[48] C. Noguera, J. Phys. Condens. Matter 12 (2000) R367–R410.
[49] K. Rapcewicz, B. Chen, B. Yakobson, J. Bernholc, Phys. Rev. B 57 (1998) 7281–7291.